# Supporting information

## Long-term stable piezocatalytic degradation via bulk $LiNbO_3$ single-crystal

*Xiangfei Sun[1], Kunfeng Chen[1,]*, Gongbin Tang[1], Andreas Ruediger[2] and Dongfeng Xue[3,]**

[1] Institute of Novel Semiconductors, State Key Laboratory of Crystal Materials, Shandong University, Jinan 250100, China

[2.] Centre Énergie Matériaux Télécommunication, Institut National de la Recherche Scientifique, 1650 Boulevard Lionel-Boulet, Varennes, Québec J3X 1P7, Canada

[3] Shenzhen Institute for Advanced Study, University of Electronic Science and Technology of China, Shenzhen 518110, China

*Corresponding author E-mail: Kunfeng.Chen@sdu.edu.cn; dfxue@uestc.edu.cn

**Materials and methods**

**Reagents and apparatus**

RhB, Mo, MB, sodium sulfate ($Na_2SO_4$), potassium hydroxide (KOH) and hydrochloride (HCl) were supplied by Sinopharm Chemical Reagent Co. Ltd (Dalian, China). All chemical reagents were analytically pure.

**Characterization of catalysts**

The phase composition of $LiNbO_3$ was measured using an X-ray diffractometer (Japan Rigaaku Rotalex) by Cu Kα radiation (λ = 1.5418 Å). Element and valence distribution were characterized using X-ray photoelectron spectroscopy (XPS, Thermo Scientific ESCALAB Xi+). UV–vis absorption spectra of $LiNbO_3$ were measured using an Ultraviolet spectrophotometer (Shimadzu UV 3600, Japan). The Fourier transform infrared (FTIR) spectra were characterized using PerkinElmer. The Raman spectra were characterized using In situ confocal Raman spectrometer (LabRAM HR Evolution, HORIBA). The electron paramagnetic resonance (EPR) tests used Bruker 500 spectrometer (Bruker E500). The piezoelectric performances were tested with an atomic force microscope (AFM, Bruker Corporation) in PFM mode.

**Piezoelectric-pyroelectric performance**

For the piezoelectric catalytic performance test, a 1 × 2 cm $LiNbO_3$ crystal was used as the catalyst, and several typical organic dyes (MB, RhB, and MO) were selected as target pollutants for

ultrasonic-driven catalytic degradation. Three organic dye solutions were first prepared at a concentration of 5 mg $L^{-1}$ and 10 mg L-1. The $LiNbO_3$ crystals were immersed in the dye solutions and kept under magnetic agitation for 30 min in the dark to reach adsorption–desorption equilibrium. Subsequently, the ultrasonic catalytic degradation was carried out in an ultrasonic cleaner operating at a frequency of 40 kHz and a power of 80 W, while the reaction temperature was maintain $15 \pm 1.5$ °C by adding ice to the ultrasonic bath to ensure thermal stability. During the catalytic process, the absorbance of the dye solution was monitored in real time using a UV-Visible spectrophotometer. Measurements were taken at fixed intervals to evaluate the catalytic activity of the $LiNbO_3$.

**Pyroelectric performance**

As in the previous process of piezoelectric and pyroelectric catalytic performance tests, dark treatment was performed to achieve an adsorption-desorption equilibrium state. The organic dye containing $LiNbO_3$ catalyst was placed alternately in two water baths at 15 ℃ and 40 ℃ respectively. After 30 minutes, the absorbance of the organic dye was measured.

**Electrochemical measurements**

$LiNbO_3$ (1×2 cm) was coated with conductive silver adhesive as the working electrode. The transient piezo-current responses, Mott-Schottky plots and electrochemical impedance spectra (EIS) were performed using CHI 660D Electrochemical Workstation. For all tests in 0.5 M $Na_2SO_4$ solution media, Hg/HgCl electrode and Pt wire were used as reference and counter electrodes, respectively.

**ATR-FTIR measurement of ultrasonic field-induced spectral shifts.**

To probe the local electric field variations induced by ultrasonic excitation, attenuated total reflection Fourier-transform infrared (ATR-FTIR) spectroscopy was performed using a Nicolet iS50 spectrometer equipped with a diamond ATR crystal. Methyl acrylate (MA) was chosen as the vibrational Stark probe owing to its strong and isolated carbonyl (C=O) stretching band near 1730 $cm^{-1}$, which is highly sensitive to electric field perturbations. Ultrasonic irradiation was applied to the solution using a probe-type sonicator (frequency ≈ 40 kH) for 1 min, while the IR spectra were recorded before and immediately after ultrasonication under identical optical settings . The frequency shift of the C=O stretching peak was extracted by fitting the band with a Gaussian function.

**DFT calculation**

Spin-polarized first-principle calculations were performed by the density functional theory (DFT) using the Vienna Ab-initio Simulation Package (VASP) package.[1] The generalized gradient approximation (GGA) with the Perdew-Burke-Ernzerhof (PBE) functional were used to describe the electronic exchange and correlation effects. [2-4] Uniform G-centered k-points meshes with a resolution of $2\pi\times0.04$ $Å^{-1}$ and Methfessel-Paxton electronic smearing were adopted for the integration in the Brillouin zone for geometric optimization. The simulation was run with a cutoff energy of 500 eV throughout the computations. These settings ensure convergence of the total energies to within 1 meV per atom. The geometry optimization was considered convergent when the electronic energy and Hellmann-Feynman forces convergence criterion was smaller than $10^{-5}$ eV and 0.03 eV $Å^{-1}$, respectively. In the calculation, Grimme's DFT-D3 [5] methodology was used to describe the dispersion interactions. A vacuum distance of 15 Å was set to ensure sufficient vacuum and avoid interactions between two periods.

**COMSOL simulation**

The piezoelectric potential distribution on the $LiNbO_3$ was simulated using COMSOL Multiphysics Software. A 3D geometry with dimensions of 500 μm×1 cm×2 cm was used, where the simulation domain was uniformly distributed. For the boundary conditions, the upper end of the cantilever was set to be free in response to the applied force.

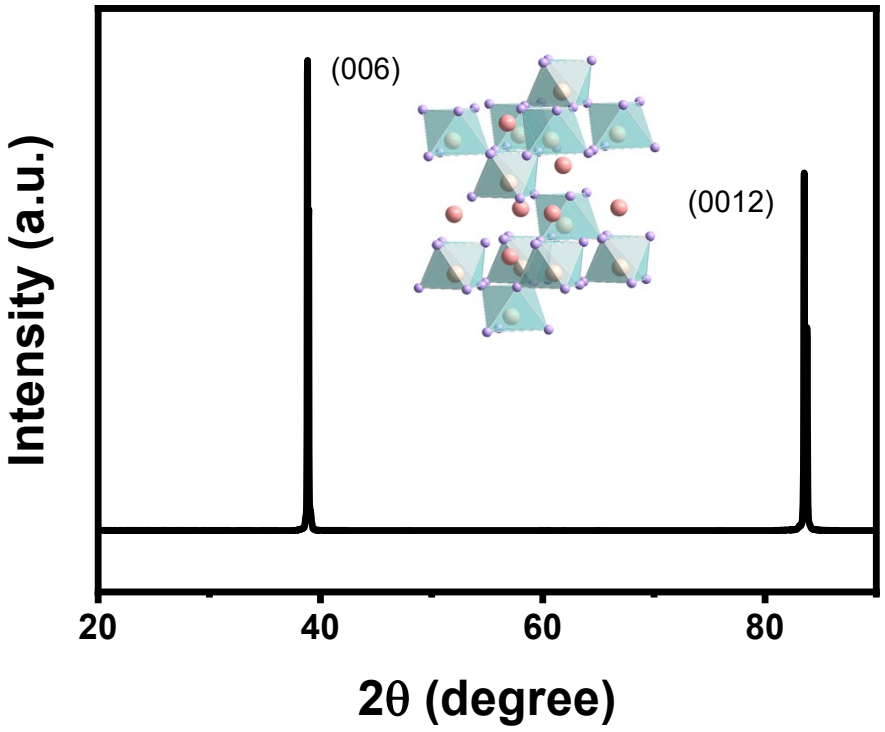


Figure S1 XRD pattern of $LiNbO_3$.

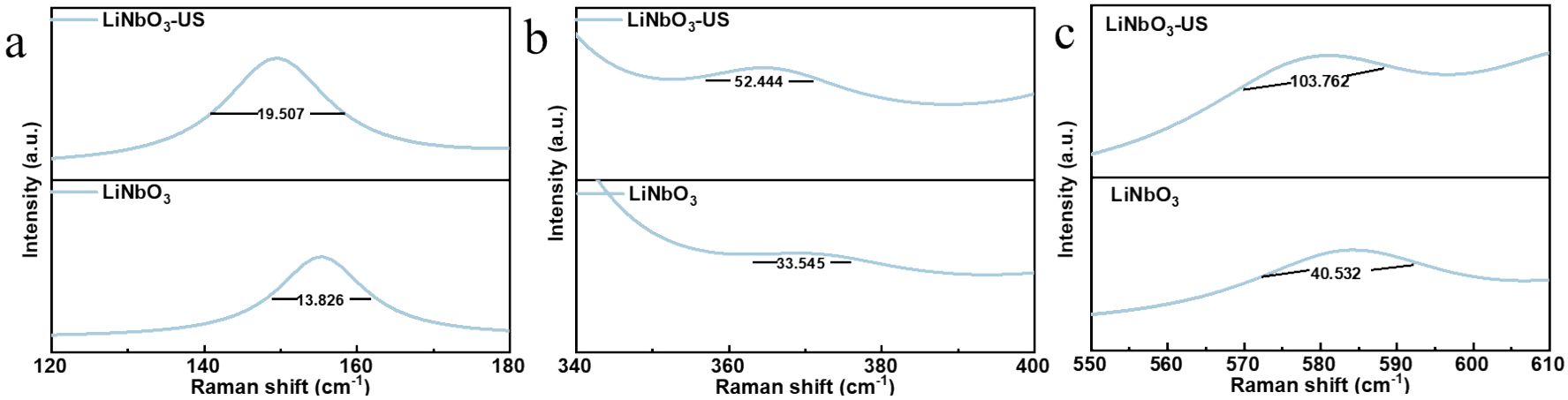


Figure S2 Raman spectra of $LiNbO_3$and $LiNbO_3$-US.

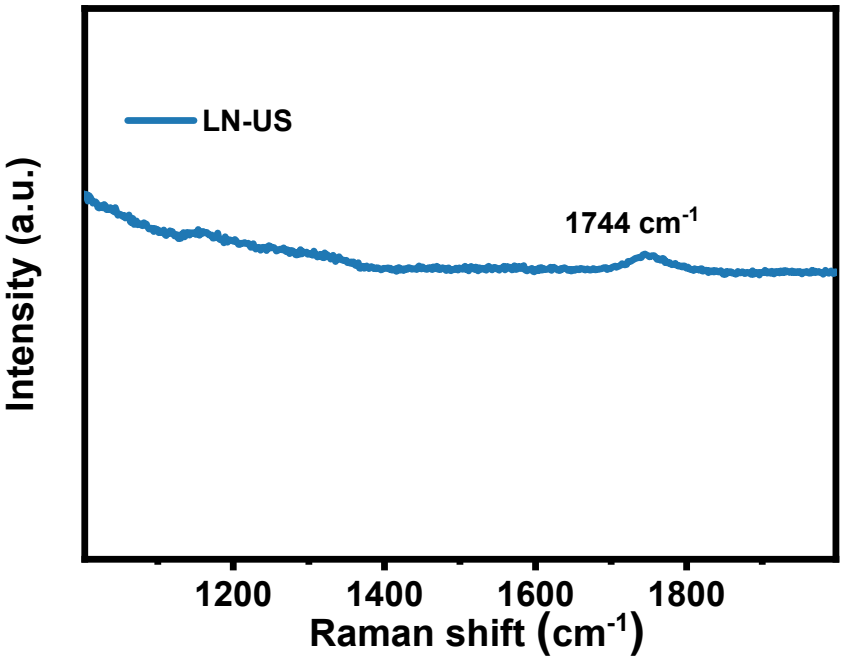


Figure S3 Raman spectra of $LiNbO_3$-US.

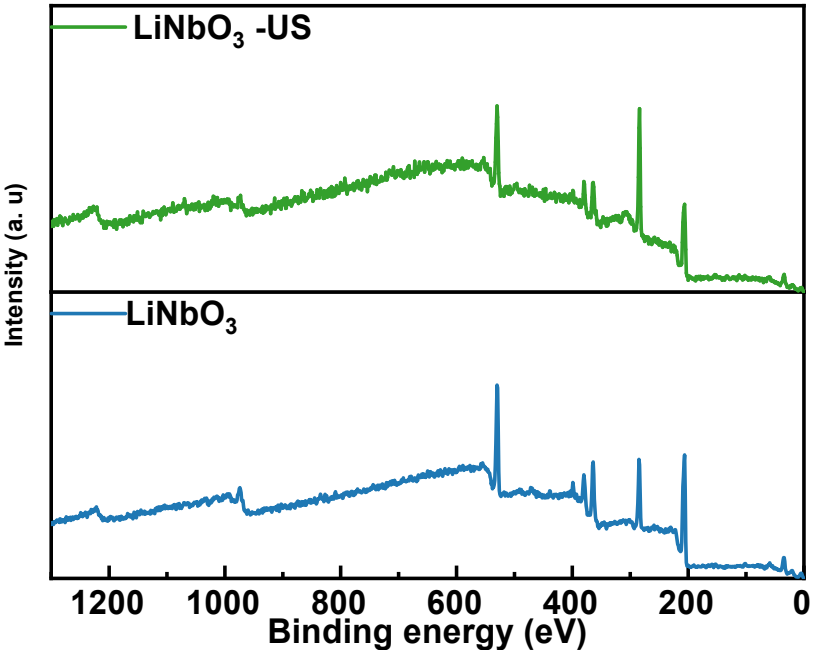


Figure S4 XPS survey spectrum of $LiNbO_3$ and $LiNbO_3$-US.

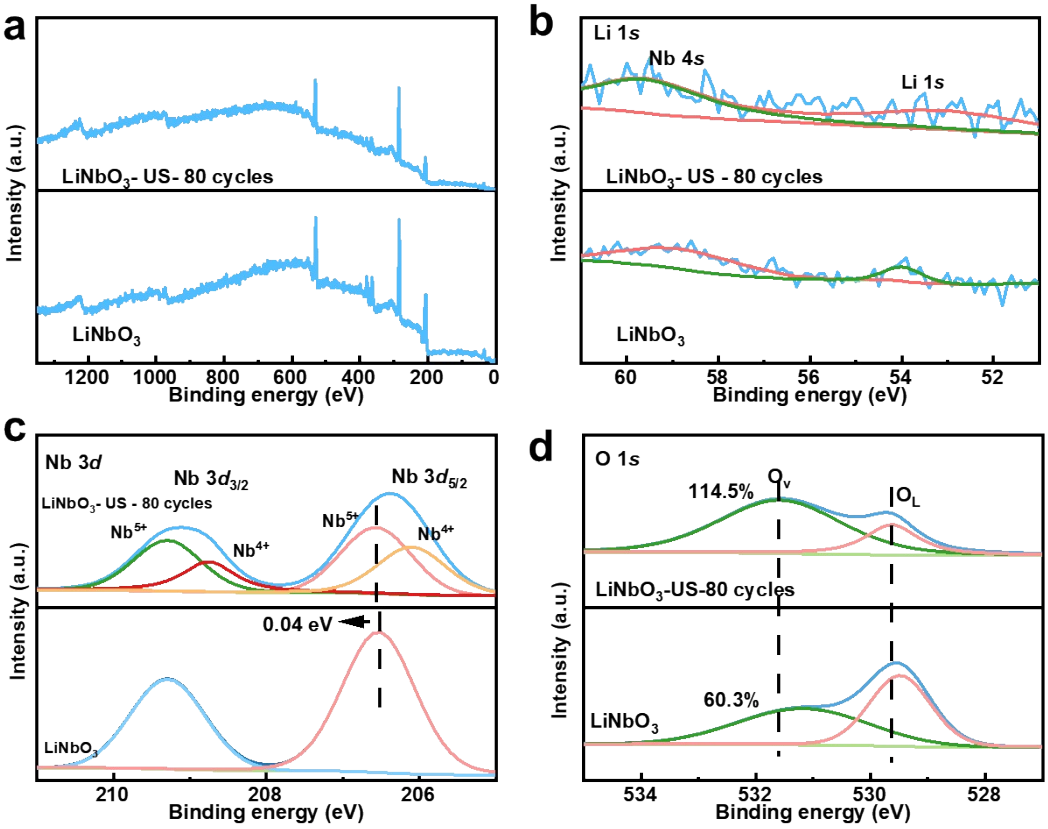


Figure S5 XPS measurements of (a) survey, (b) Li 1*s* high-resolution XPS spectra, (c) Nb 3*d* high-resolution XPS spectra, (d) O 1*s* high-resolution spectra of $LiNbO_3$-US-80 cycles

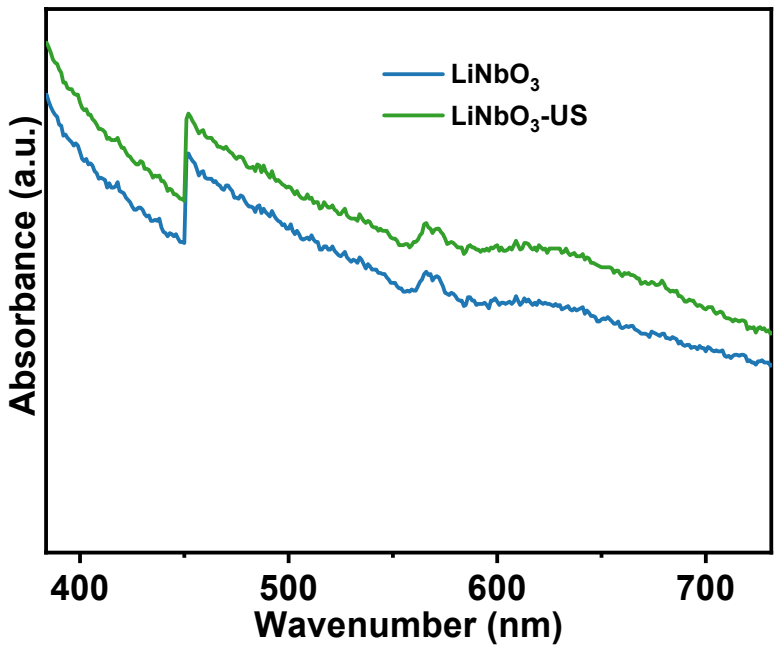


Figure S6 UV-Vis spectra of $LiNbO_3$ and $LiNbO_3$-US (Figure 1g, enlarged image in

the visible light region).

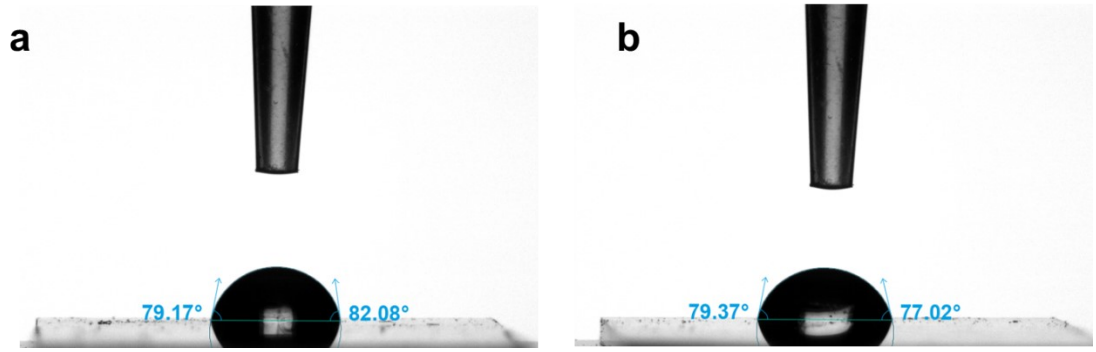


Figure S7 Contact angles of water droplets on the surface of (a) $LiNbO_3$ and (b) $LiNbO_3$-US

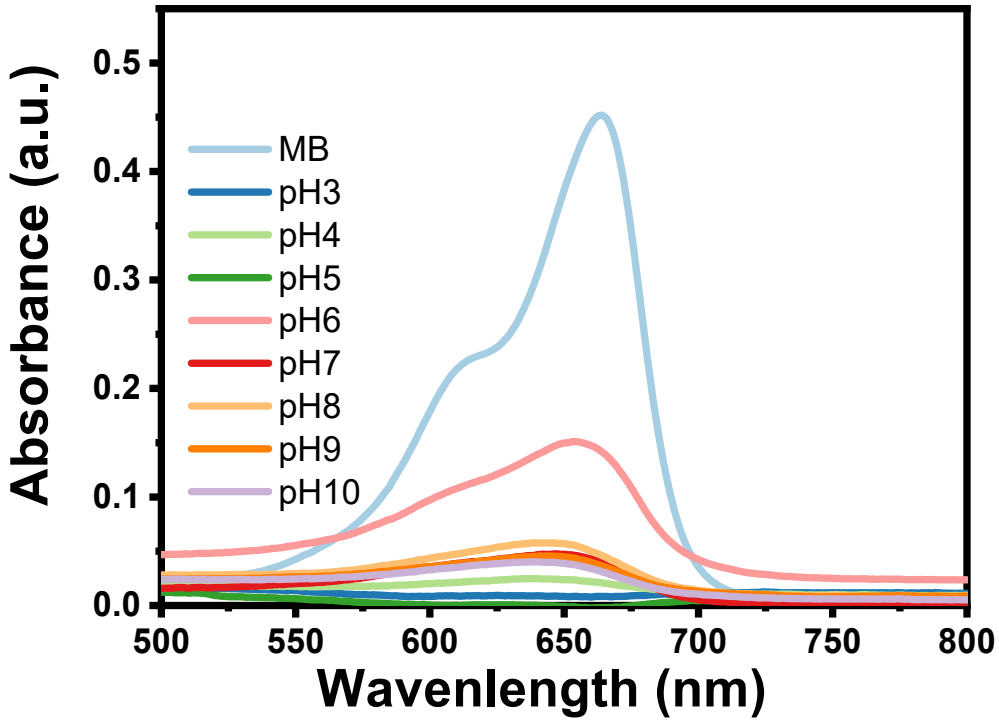


Figure S8. UV-vis absorbance of RhB under ultrasonic vibration at different pH values.

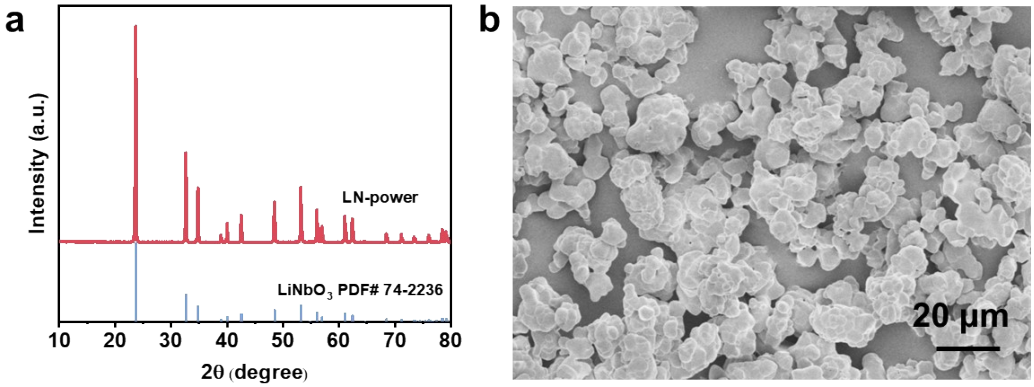


Figure S9 XRD and SEM image of $LiNbO_3$ power

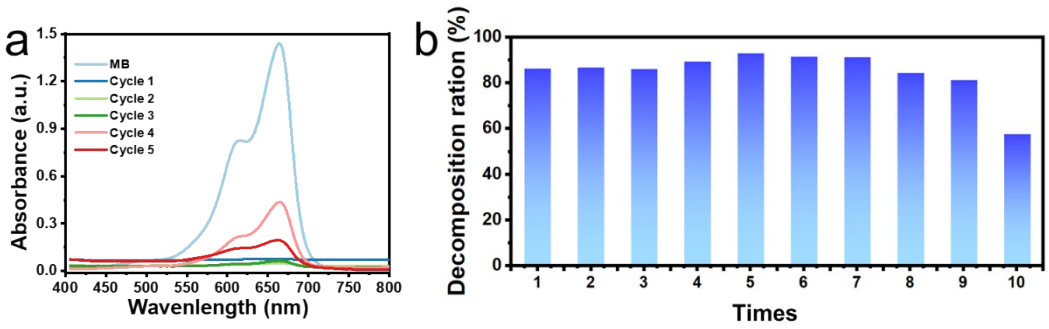


Figure S10. Recycling ability of the $LiNbO_3$ for degrading RhB

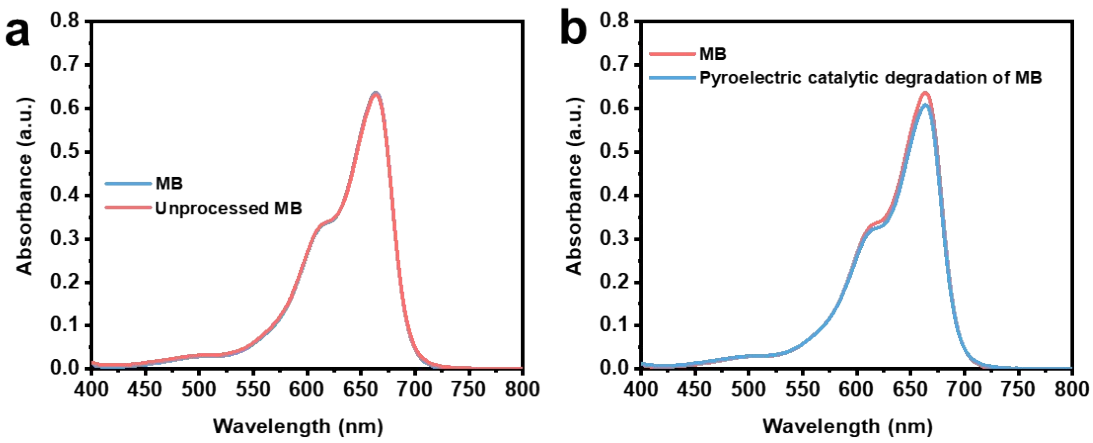


Figure S11. UV-vis absorbance of MB under untreated (a) and heat-treated conditions (b).

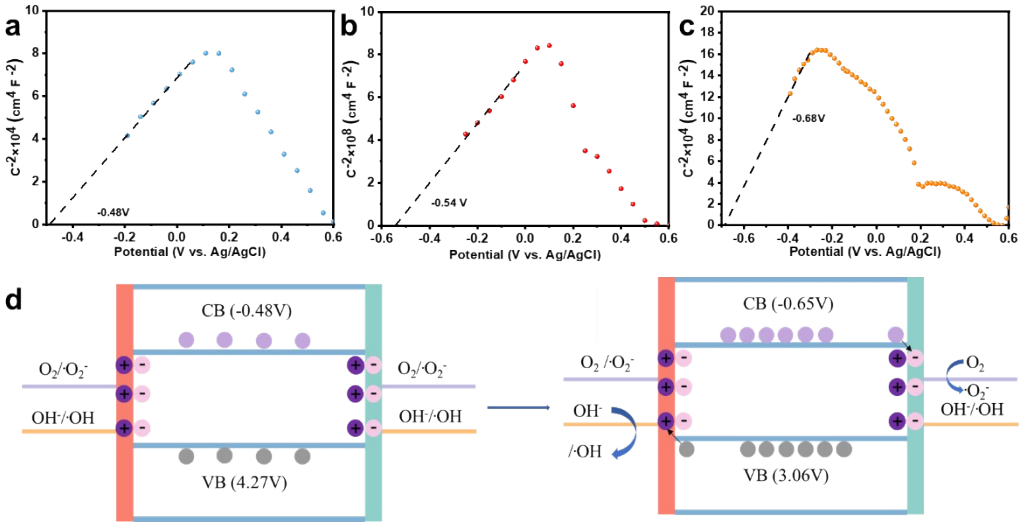


Figure S12. Mott-Schottky plots of $LiNbO_3$ at room temperature (a), 40℃ water bath (b) and ultrasound (c)

Table S1. A comparison of organic dyes was compared to catalytic degradation properties by using different piezoelectric catalysts.

| Piezocatalyst | Dye species | Dye concentration (mg $L^{-1}$) | Ultrasonic Energy source | Rate constant (min $L^{-3}$) | cycling performance | Refs |
|---|---|---|---|---|---|---|
| BT nanowires | MO | 5 | 40 kHz, 80W | 15 | 4 | [6] |
| Li-modified KNN nanoparticles | RhB | 5 | 40 kHz, 300W | 25.16 | 8 | [7] |
| $BaTiO_3$-$TiO_2$ | IC | 10 | 100 kHz, 200W + Light: 300 W | 110 | 8 | [8] |
| BiOBr/$BaTiO_3$ | MB | 10 | 40 kHz, 120W | 15.5 | 7 | [9] |
| $Bi_{25}FeO_{40}$/$Bi_2O_2CO_3$ | 4-chlorophenol | 10 | 40 kHz, 120W | | 3 | [10] |
| BNT nanorods | RhB | 5 | 28 kHz, 100W + Light:300 W | 94 | 8 | [11] |
| $LiNbO_3$ | RhB | 5 | 40 kHz, 80 W | 102 | 80 | This work |

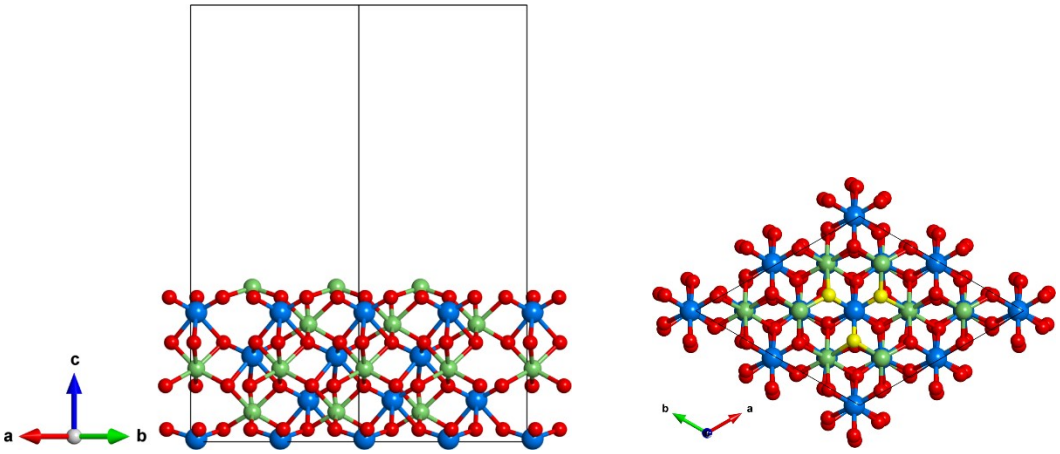


(a) Side view (b) Top view

**Figure S13** Side and top view of $LiNbO_3$ (001) surface, the yellow balls denote the O vacancy sites. Li: green; Nb: blue; O: red.

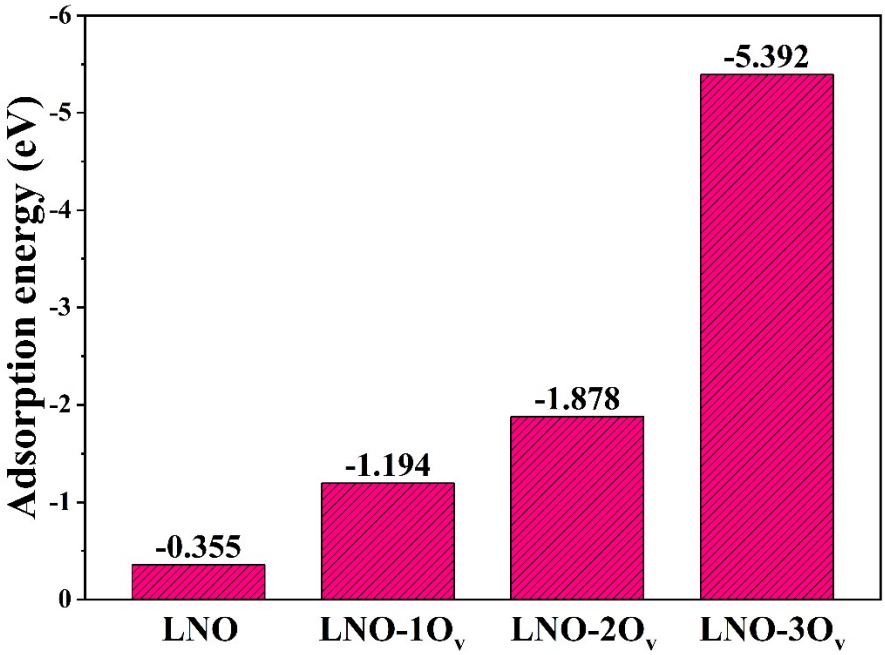


**Figure S14** Calculated adsorption energy of $O_2$ molecules on $LiNbO_3$, $LiNbO_3$-1 $O_V$, $LiNbO_3$-2 $O_V$, $LiNbO_3$-3 $O_V$

Table S2 The calculated adsorption energy of $O_2$ on $LiNbO_3$, $LiNbO_3$-1$O_v$, $LiNbO_3$-2$O_v$, $LiNbO_3$-3$O_v$ surfaces of $LiNbO_3$ (001) (unit: eV).

| | $E_{(total)}$ | $E_{(surface)}$ | $E_{(O2)}$ | $\Delta E_{ads}$ |
|---|---|---|---|---|
| $LiNbO_3$ | -640.53023343 | -630.31739124 | -9.85801363 | -0.35482856 |
| $LiNbO_3$-1$O_v$ | -636.25856258 | -625.20646470 | -9.85801363 | -1.19408425 |
| $LiNbO_3$-2$O_v$ | -629.81270630 | -618.07706233 | -9.85801363 | -1.87763034 |
| $LiNbO_3$-3$O_v$ | -623.86042798 | -608.61020845 | -9.85801363 | -5.39220590 |

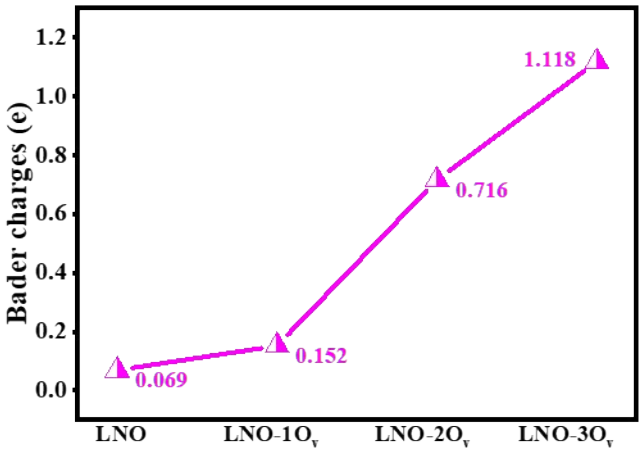


**Figure S15**The calculated bader charges of $O_2$ adsorbed on $LiNbO_3$, $LiNbO_3$-1 $O_V$, $LiNbO_3$-2 $O_V$, $LiNbO_3$-3 $O_V$.

Table S3 The calculated bader charges of $O_2$ adsorbed on $LiNbO_3$, $LiNbO_3$-1$O_v$, $LiNbO_3$-2$O_v$, $LiNbO_3$-3$O_v$ surfaces of $LiNbO_3$ (001).

| | $Q_{(O2)}$ |
|---|---|
| $LiNbO_3$ | -0.069 |
| $LiNbO_3$-1$O_v$ | -0.152 |
| $LiNbO_3$-2$O_v$ | -0.716 |
| $LiNbO_3$-3$O_v$ | -1.118 |

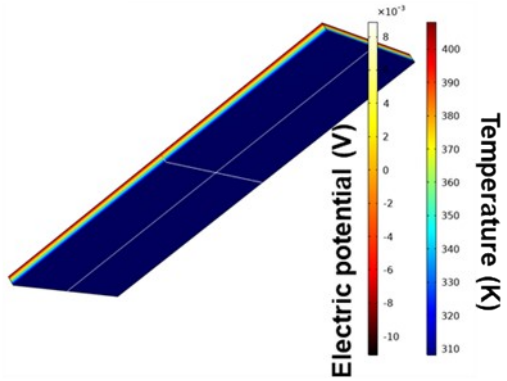


**Figure S16**. COMSOL simulation for the piezoelectric potential distribution in $LiNbO_3$ under thermal treatment

[1] G. Kresse, J. Furthmüller. Efficiency of ab - initio total energy calculations for metals and semiconductors using a plane - wave basis set. Comput. Mater. Sci. 1996, 6, 15 - 50.

[2] K. Burke, M. Ernzerhof, J. P. Perdew. Generalized Gradient Approximation Made Simple. Phys. Rev. Lett. 1996, 77, 3865 - 3868.

[3] P. E. Blöchl. Projector augmented - wave method. Phys. Rev. B 1994, 50, 17953 - 17979.

[4] G. Kresse, D. P. Joubert. From ultrasoft pseudopotentials to the projector augmented - wave method. Phys. Rev. B 1999, 59, 1758 - 1775.

[5] S. Grimme, S. Ehrlich, L. Goerigk. Effect of the damping function in dispersion corrected density functional theory. J. Comput. Chem. 2011, 32, 1456 – 1465.

[6] J. Wu, N. Qin, D. Bao. Effective enhancement of piezocatalytic activity of $BaTiO_3$ nanowires under ultrasonic vibration. Nano Energy 2018, 45, 44 - 51.

[7] A. Zhang, Z. Liu, B. Xie, J. Lu, K. Guo, S. Ke, L. Shu, H. Fan. Vibration catalysis of eco - friendly $Na_{0.5}K_{0.5}NbO_3$ - based piezoelectric: An efficient phase boundary catalyst. Appl. Catal. B: Environ. 2020, 279, 119353.

[8] Q. Liu, Z. Li, J. Li, F. Zhan, D. Zhai, Q. Sun, Z. Xiao, H. Luo, D. Zhang. Three dimensional $BaTiO_3$ piezoelectric ceramics coated with $TiO_2$ nanoarray for high performance of piezo - photoelectric catalysis. Nano Energy 2022, 98, 107267.

[9] X. Zhou, F. Yan, S. Wu, B. Shen, H. Zeng, J. Zhai. Remarkable Piezophoto Coupling Catalysis Behavior of BiOX/$BaTiO_3$ (X = Cl, Br, $Cl_{0.166}Br_{0.834}$) Piezoelectric Composites. Small 2020, 16, 2001573.

[10] T. Jiang, Y. Wang, Z. Guo, H. Luo, C. Zhan, Y. Wang, Z. Wang, F. Jiang, H. Chen. $Bi_{25}FeO_{40}/Bi_2O_2CO_3$ piezoelectric catalyst with built - in electric fields that was prepared via photochemical self - etching of $Bi_{25}FeO_{40}$ for 4 - chlorophenol degradation. Journal of Cleaner Production 2022, 341, 130908.

[11] X. Zhou, Q. Sun, D. Zhai, G. Xue, H. Luo, D. Zhang. Excellent catalytic performance of molten - salt - synthesized $Bi_{0.5}Na_{0.5}TiO_3$ nanorods by the piezo - phototronic coupling effect. Nano Energy 2021, 84, 105936.